**Article**

# A bimetallic-activated MnO₂ self-assembly electrode with a dual heterojunction structure for high-performance rechargeable zinc-air batteries

**Zhengyu Yin[1,#], Rui He[1,#], Huaibin Xue[2], Jingjian Chen[1], Yue Wang[1], Xiaoxiao Ye[1], Nengneng Xu[1,\*], Jinli Qiao[1,3,\*], Haitao Huang[4,\*]**

[1]State Key Laboratory for Modification of Chemical Fibers and Polymer Materials, College of Environmental Science and Engineering, Donghua University, Shanghai 201620, China.
[2]Shanghai Jinyuyuan Clean-Energy Technology Co., Ltd., Shanghai 201208 China.
[3]Shanghai Institute of Pollution Control and Ecological Security, Shanghai 200092, China.
[4]Department of Applied Physics, Hong Kong Polytechnic University, Hong Kong, China.
[#]Authors contributed equally.

[\*]**Correspondence to:** Prof. Jinli Qiao, State Key Laboratory for Modification of Chemical Fibers and Polymer Materials, College of Environmental Science and Engineering, Donghua University, 2999 Ren'min North Road, Shanghai 201620, China. E-mail: qiaojl@dhu.edu.cn; Dr. Nengneng Xu, College of Environmental Science and Engineering, Donghua University, 2999 Ren'min North Road, Shanghai 201620, China. E-mail: nengnengxu@dhu.edu.cn; Prof. Haitao Huang, Department of Applied Physics, Hong Kong Polytechnic University, 11 Yucai Road, Kowloon, Hong Kong, China. E-mail: aphhuang@polyu.edu.hk.

## Abstract

A major challenge in developing zinc-air batteries (ZABs) is to exploit suitable cathodes to efficiently accelerate the key electrocatalytic processes involved. Herein, a bifunctional oxygen catalytic self-supported MnO₂-based electrode is designed that displays superior oxygen reduction and evolution reaction performance over noble metal electrodes with a total overpotential of 0.69 V. In addition, the as-synthesized NiCo₂O₄@MnO₂/carbon nanotube (CNT)-Ni foam self-supported electrode can be directly used as an oxygen electrode without externally adding carbon or a binder and shows reasonable battery performance with a high peak power density of 226 mW cm⁻² and a long-term charge-discharge cycling lifetime (5 mA for 160 h). As expected, the rapid oxygen catalytic intrinsic kinetics and high battery performance of the NiCo₂O₄@MnO₂/CNTs-Ni foam electrode originates from the unique three-dimensional hierarchical structure, which effectively promotes mass transfer. Furthermore, the CNTs combined with Ni foam form a unique "meridian" conductive structure that enables rapid electron conduction.

Finally, the abundant $Mn^{3+}$ active sites activated by bimetallic ions shorten the oxygen catalytic reaction distance between the active sites and reactant and reduce the surface activity of $MnO_2$ for the O, OH, and OOH species. This work not only offers a high-performance bifunctional self-supported electrode for ZABs but also opens new insights into the activation of Mn-based electrodes.

**Keywords:** Zinc-air batteries, bimetallic activation, self-supported electrode, heterojunction, hierarchical structure

## INTRODUCTION

Zinc-air batteries (ZABs) have attracted significant interest due to their strong competitiveness in terms of cost, safety, and energy density[1-6]. However, the sluggish dynamics of the oxygen reduction reaction (ORR) and oxygen evolution reaction (OER) occurring at the cathode severely limit the charge-discharge performance and efficiency of ZABs. Although substantial work has been carried out on the synthesis of noble metal powder catalysts (e.g., Pt/C and $IrO_2$) for the ORR and OER, the scarcity and unsatisfactory bifunctionality of noble metals severely reduce the possibility of their large-scale applications[1,7]. Thus, it is particularly necessary to develop low-cost and highly efficient non-precious metal bifunctional catalysts for the ORR and OER.

$\alpha$-$MnO_2$-based catalysts remain the most promising non-noble oxygen catalytic reaction candidates in alkaline electrolytes, owing to their unique layered and 2 × 2 tunnel structures[3,8,9]. Generally, the basic structural lattice framework of $\alpha$-$MnO_2$ is a corner-/edge-sharing $[MnO_6]$ octahedral unit and a Mn oxidation state of $4^+$[10]. In $O_2$ catalytic reactions, $Mn^{3+}$, cyclically produced by the $Mn^{4+}$ reduction, serves as the active site to form the $O_2$ intermediate by combining with $O_2$, which is the rate-determining step[11,12]. However, the formed $Mn^{3+}$ still occupies the octahedral sites of the $[MnO_6]$ units and exists with unpaired single electrons at the high spin electronic energy $e_g$ band ($Mn^{3+}$, $t_{2g}3$, $e_g1$), which shows extremely low thermodynamic stability[12]. Accordingly, obtaining abundant and stable $Mn^{3+}$ is of great significance for designing high-performance Mn-based bifunctional catalysts. In recent decades, several valuable strategies have been proposed to further enhance the performance of $\alpha$-$MnO_2$-based catalysts, such as coupling other transition metal oxides to construct unique heterojunction structures[13-15]. For example, a $Co_3O_4$-$MnO_2$/carbon nanotube (CNT) hybrid exhibited a significant increase in $Mn^{3+}$ density and a concomitant decrease in electron energy due to the bonding of the bottom Co atoms to the surface O on the $MnO_2$ surface[13]. As a result, the $Co_3O_4$-$MnO_2$/CNT hybrid showed good ORR and OER performance. However, there are still two major issues for Mn-based catalysts manipulated by the unary spinel: (1) the electronic configuration of the Co-Mn heterojunction needs to be further modulated[16]; and (2) the inherent limitations of powder catalysts still need to be overcome (e.g., significant dead volume, an undesirable three-phase reaction interface and uncontrolled microstructures).

Some studies reported that partially replacing the Co element of $Co_3O_4$ in $Co_3O_4$-$MnO_2$/CNT hybrids with nickel can reduce the particle size and increase the Co-Mn heterojunction density, which contributes to the activity and the long-term durability of the catalyst[14,17,18]. In particular, the interaction force between the low-spin $Co^{3+}$ in the octahedral site and the oxygen intermediate can be weakened by the partial substitution of Ni atoms[19,20]. Thus, the bond length of Co-Mn-O can be further modulated by coupling the $NiCo_2O_4$ binary spinel instead of $Co_3O_4$[21]. In contrast, achieving the self-support of active species on conductive substrates can effectively avoid the limitations of powder catalysts[22,23]. On this basis, it has become more attractive to synthesize high-performance $NiCo_2O_4$/$MnO_2$ self-supported bifunctional electrodes. The advantages of such a new self-supported bifunctional electrode include: (1) the construction of a high electron transfer pathway via *in situ* growth of the conductive substrates with electroactive species. The *in*

*situ* self-fabrication procedure assures good conductivity and high mechanical stability of the electrode, which does not require the post-costing process and additional organic binders[24]; (2) a possibly rapid intrinsic kinetics and long-term durability due to the stable double heterojunction structure ($NiCoO_x$-$MnO_2$ and $MnO_2$ substrate) and the activation of Mn sites[14]; and (3) rapid mass transfer (e.g., the ion diffusion and the emission of the reaction products) at the three-phase reaction interface, which should be attributed to the formation of the open space within a three-dimensional (3D) nanostructured array network[25]. Notably, a bimetallic-activated $MnO_2$ self-supported electrode has not yet been explored in ZABs.

Hence, inspired by the aforementioned considerations, we design a useful strategy to construct a bimetallic-activated $MnO_2$-based electrode by a self-assembly process. During this process, $NiCo_2O_4$-bound CNTs (a nanosheet) along the self-assembled $MnO_2$ arrays on the surface of the nickel foam form a unique tremella-like 3D hierarchical structure with an abundant heterojunction ($NiCo_2O_4$@$MnO_2$/CNTs-Ni foam). The unique 3D hierarchical structure effectively promotes electrolyte penetration, reactant ($O_2$ and $OH^-$) diffusion, and product emission, consequently facilitating the ORR and OER kinetics. In particular, the intrinsic activity of oxygen catalysis is further enhanced by the strategy of introducing nickel foam to form abundant $Mn^{3+}$ active sites and utilizing bimetallic activation of the active sites to reduce the surface activity of $MnO_2$ for the O, OH, and OOH species. As expected, the as-prepared $NiCo_2O_4$@$MnO_2$/CNTs-Ni foam self-supporting electrode exhibits good OER and ORR performance with an ultralow total overpotential of 0.69 V. The $NiCo_2O_4$@$MnO_2$/CNTs-Ni foam-based ZABs show a high peak power density of 226 mW cm$^{-2}$ at 0.74 V, which is superior to Pt/C-$RuO_2$ (93 mW cm$^{-2}$ at 0.47 V). Additionally, the $NiCo_2O_4$@$MnO_2$/CNTs-Ni foam electrode also displays long-term charge-discharge cycling stability, which should be attributed to the stable 3D hierarchical hollow hybrid structure and the active sites. This study provides a simple strategy to construct 3D hierarchical hollow hybrids and affords implications for the interface engineering field of high-performance catalysts.

## RESULTS AND DISCUSSION

As shown in Figure 1A, the $NiCo_2O_4$@$MnO_2$/CNTs-Ni foam electrode was synthesized via a facile hydrothermal coupled calcination approach. The SEM image in Figure 1B illustrates that the $NiCo_2O_4$@$MnO_2$/CNTs-Ni foam synthesized at 160 °C for 6 h has a tremella-like 3D hierarchical structure with a pore size of ~0.4 μm. This hollow porous structure is believed to not only be beneficial for buffering the volume change induced by charge-discharge cycling but also to accelerate the penetration of the electrolyte, the diffusion of OH to the electrode surface, and the rapid dissociation of the reaction products. However, when the reaction time is less than 6 h, it is difficult to form this tremella-like 3D hierarchical structure, and when the reaction time is higher than 6 h, the structure is destroyed [Supplementary Figure 1]. This is mainly due to the thermodynamic conditions during the synthesis. When the reaction time is too short, its thermodynamic environment cannot perform the process of $MnO_2$ self-assembly, and when the reaction time is too long, the excess energy will dissolve to form nanosheets.

The structural information for the catalysts was obtained by TEM. As shown in Figure 1C, the $NiCo_2O_4$/CNT nanolayered structure can be well synthesized using the second hydrothermal self-assembly process at 160 °C for 6 h. Considerable $NiCo_2O_4$/CNT nanolayered structures with an average thickness of 30 nm wrap around the $MnO_2$ nanotubes. $MnO_2$ nanotubes were introduced into the $NiCo_2O_4$/CNT hybrid catalytic system and served as its skeleton. The distribution of the individual phases was studied by HRTEM analysis. The lattice spacings in Figure 1D and E are 0.69, 0.22, and 0.24 nm, corresponding to the (110) plane of a-$MnO_2$ and the (222) and (311) planes of $NiCo_2O_4$, respectively. The SAED pattern [Figure 1F] results are consistent with those of the XRD analysis [Supplementary Figure 2], indicating a nickel-cobalt bimetallic composite of oxides and α-$MnO_2$. The XRD characteristic peaks in Supplementary Figure 2 are
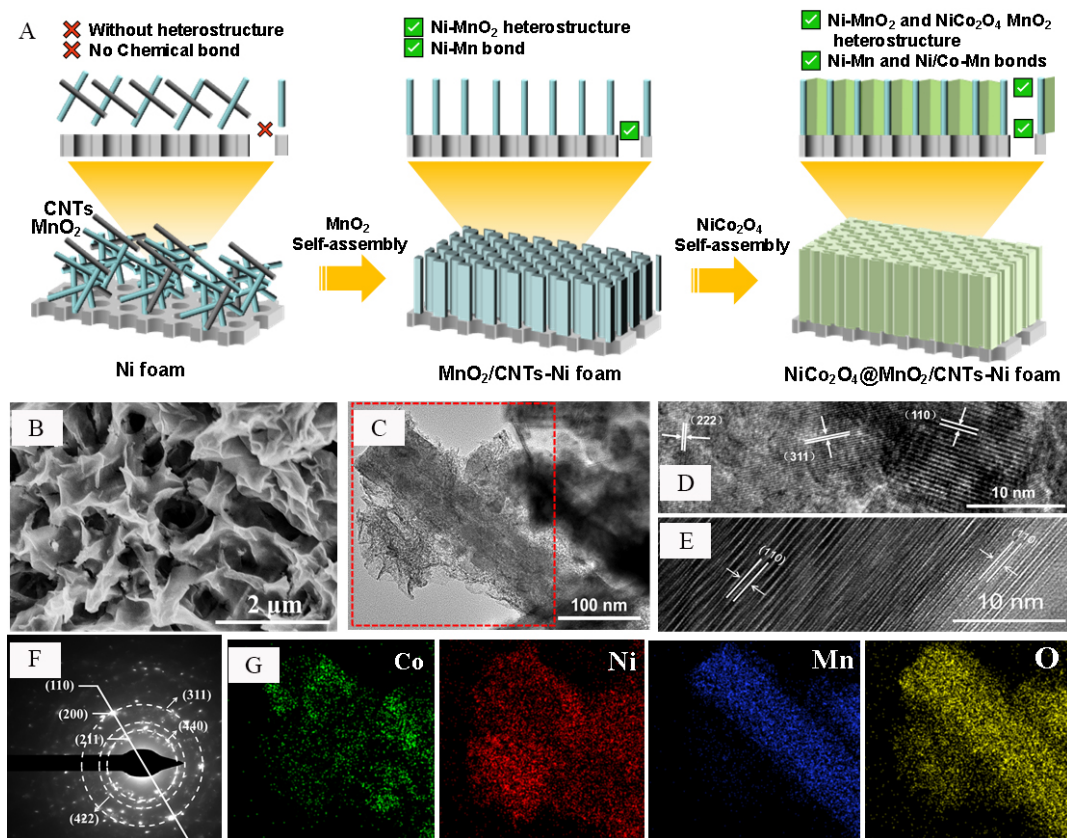
**Figure 1.** (A) Schematic of $NiCo_2O_4@MnO_2$/CNTs-Ni foam synthesis. (B) Scanning electron microscope (SEM) image of $NiCo_2O_4$ $@MnO_2$/CNTs-Ni foam. (C) Transmission electron microscope (TEM) image of $NiCo_2O_4@MnO_2$/CNTs-Ni foam. (D) and (E) High-resolution transmission electron microscopy (HRTEM) images of $NiCo_2O_4@MnO_2$/CNTs-Ni foam. (F) Selected area electron diffraction (SAED) image of $NiCo_2O_4@MnO_2$/CNTs-Ni foam. (G) Elemental (Co, Ni, Mn and O) mapping of the area within the red dotted box in Figure 1C.

contributed by $\alpha$-$MnO_2$ and $NiCo_2O_4$. This result proves that the Ni/Co bimetallic oxide synthesized by this method is $NiCo_2O_4$. Co, Ni, O, and Mn are uniformly distributed, as confirmed by the TEM elemental mappings shown in Figure 1G.

In order to gain a deeper understanding of the self-assembly process of the $NiCo_2O_4@MnO_2$/CNTs-Ni foam, the SEM images of $NiCo_2O_4$, the $Co_3O_4@MnO_2$-CNT@Ni foam, $Co_3O_4$/$MnO_2$-CNTs, and $MnO_2$ were obtained. As shown in Supplementary Figure 3, the length of the pure $MnO_2$ tubes approaches 500 nm with a width of 50 to 100 nm. For the $NiCo_2O_4$ composites prepared at the same synthesis conditions without $MnO_2$ and Ni foam, the diameter of the $NiCo_2O_4$ spheres is ~500 nm and they are huddled together tightly. When doped only with Co ions ($Co_3O_4$/$MnO_2$-CNTs) without Ni foam, the $Co_3O_4$ particles are sparsely arranged on the surface of $MnO_2$. In contrast, for Co and Ni ions ($NiCo_2O_4$/$MnO_2$-CNTs) without Ni foam, the $NiCo_2O_4$ nanoparticles wrap on the surface of the $MnO_2$ nanotubes densely and uniformly. The size of the $NiCo_2O_4$ particles (25 nm) on the $MnO_2$ nanotubes is 25 times smaller than that of pure $NiCo_2O_4$ (500 nm). Smaller particle sizes tend to provide better structural stability and larger surface areas, thereby further facilitating the electrode activity[26]. Although the catalyst has been improved with regards to size and dispersibility, deficiency of the active sites still exists caused by random gatherings of the nanoparticles. When the Ni foam is introduced to the catalyst synthesis process, these nanoparticles self-assemble with CNTs along the $MnO_2$ nanotubes to build a unique 3D network structure. In addition, the $Co_3O_4@MnO_2$
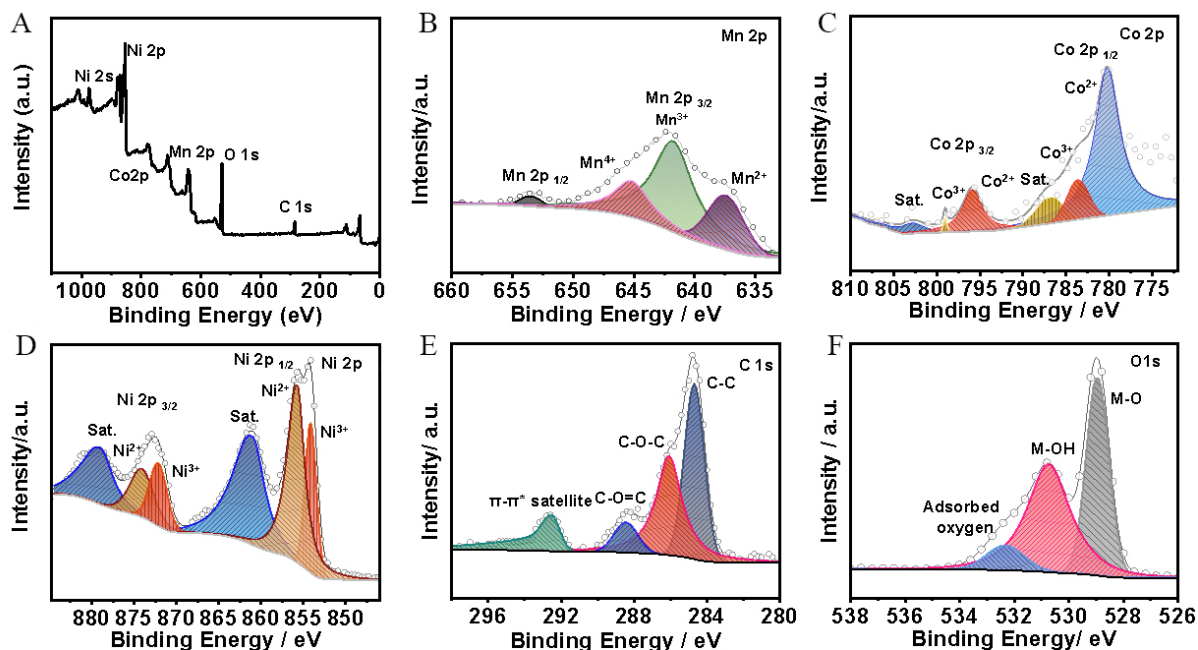
/CNTs-Ni foam [Supplementary Figure 3] also shows a similar tremella-like 3D hierarchical hollow hybrid structure as the nickel-cobalt bimetallic oxide composite.

The above findings reveal the importance of the Ni substrate, which can significantly reduce the size of the metal oxides by forming a steric hindrance effect during the self-assembling process, as well as avoiding the agglomeration of metal oxides and forming an abundant metal oxide-$MnO_2$ heterojunction structure[27,28]. Ni foam can also provide growth sites for the self-assembly of $MnO_2$, avoid the agglomeration of $MnO_2$ and form the Ni foam-$MnO_2$ heterojunction structure. Furthermore, it can induce the evolution of the nanoparticles on the surface of $MnO_2$ into two-dimensional nanosheets, thereby realizing the rapid transformation of the metal oxide-$MnO_2$ heterojunction in structure and density. This dense heterojunction structure forms an abundant three-phase reaction interface.

The XPS survey scan of the $NiCo_2O_4$@$MnO_2$/CNTs-Ni foam confirms the presence of Mn, Co, Ni, C, and O elements [Figure 2A]. As shown in Figure 2B, for the spectrum of Mn 2p, the characteristic peaks of 640-650 eV and 650-660 eV belong to Mn 2p3/2 and Mn 2p1/2, respectively. The Mn 2p3/2 spectrum is deconvoluted into three peaks. The peaks located at 645.2, 641.4, and 638.2 eV are attributed to $Mn^{4+}$, $Mn^{3+}$, and $Mn^{2+}$, respectively. $Mn^{3+}$ is widely regarded as the active center for the oxygen-catalyzed reaction. Notably, the proportion of $Mn^{3+}$ in the $NiCo_2O_4$@$MnO_2$/CNTs-Ni foam is 55.8%, which is higher than for pure $MnO_2$ (0%, Supplementary Figure 4A), the $NiCo_2O_4$@$MnO_2$/CNTs-Ni foam catalyst (0%, Supplementary Figure 4B) and the $Co_3O_4$@$MnO_2$-CNT@Ni foam (36.4%, Supplementary Figure 4C). Therefore, for the Ni-based self-supporting electrode, the introduction of Ni foam is beneficial to the existence of Mn ions in the form of $Mn^{3+}$, which will effectively increase the active site density of the catalytic system.

In addition, compared with the normal Mn 2p peaks (641.8 eV for Mn 2p3/2 and 653.5 eV for Mn 2p1/2), the main Mn 2p peaks (641.4 eV and 652.9 eV) in the $NiCo_2O_4$@$MnO_2$/CNTs-Ni foam shift to a lower binding energy. The binding energy shift should be caused by the transfer of electrons from $NiCo_2O_4$ to the $MnO_2$ surface and the heterojunction formation of $NiCo_2O_4$-$MnO_2$. The electrons obtained from $NiCo_2O_4$ activate the active site on the surface of $MnO_2$ by moving the Mn electron cloud to a lower energy, thereby further enhancing the ORR and OER activities[29,30]. Specifically, in comparison to the $Co_3O_4$@$MnO_2$-CNT@Ni foam, the $NiCo_2O_4$@$MnO_2$/CNTs-Ni foam modified by Ni ions showed a stronger active center activation effect on $MnO_2$ by changing the strength of the Ni-Co-O-Mn bond[14]. The Ni-Co-O-Mn bond can be significantly controlled by substituting $Co^{2+}$ at tetrahedral sites with Ni ions[18]. Overall, the change in the Mn state may be due to the abundant Ni ions provided by the Ni foam and nitrate (especially Ni foam).

Figure 2C shows the Co 2p spectrum, with two peaks observed for Co 2p1/2 and Co 2p3/2 at ~790-800 eV and ~775-785 eV, respectively[31]. For the unfolded spectra, the peaks located at 798.9 and 795.8 eV are considered as $Co^{3+}$ and $Co^{2+}$, respectively, with the remaining two peaks at 783.5 and 780.1 eV also corresponding to $Co^{3+}$ and $Co^{2+}$. In addition, the Ni 2p spectra can be deconvoluted into 2 paired peaks of $Ni^{2+}$ (874.0 and 855.9 eV)/$Ni^{3+}$ (872.1 and 854.0 eV) with an energy separation of 18.1 eV, as well as two shakeup satellites (879.3 and 861.2 eV) [Figure 2D][32]. In addition, the intense peak of the C 1s spectrum [Figure 2E] at 284.6 eV is assigned to the $sp^2$ C-C bond[33,34]. The other two weak peaks at 286.1 and 288.4 eV correspond to the C-O-C bonds and O-C=O functionalities, respectively[35]. The O 1s spectra of the $NiCo_2O_4$/$MnO_2$-CNT@Ni foam can be deconvoluted into three main peaks, which correspond to surface lattice oxygen (M-O (M = NiCo, Mn) bond at 529.2 eV), surface hydroxyls and adsorbed $H_2O$, respectively [Figure 2F][36]. Similar to Mn 2p, the ratios of hydroxyl oxygen in the $NiCo_2O_4$@$MnO_2$/CNTs-Ni and $Co_3O_4$@$MnO_2$/CNTs-Ni foams are significantly increased after the introduction of nickel foam, which is higher

**Figure 2.** (A) Overall XPS spectrum of NiCo$_2$O$_4$@MnO$_2$/CNTs-Ni foam. High-resolution curves of (B) Mn 2p, (C) Co 2p, (D) Ni 2p, (E) C 1 s and (F) O 1 s regions.

than for MnO$_2$ and NiCo$_2$O$_4$/MnO$_2$-CNTs [Supplementary Figure 4D-F]. Notably, owing to the H$_2$O decomposition ability of the surface metal species, numerous surface hydroxyl groups can be formed on the surface of the catalyst, which is essential for increasing the active sites and promoting the OER performance.

For the ORR and OER, the bimetallic activation effect caused by the construction of the abundant heterojunction of the self-supported electrode significantly decreases the hydrogen bonding with OH and OOH. In addition, the rich Mn$^{3+}$ ions as the active sites further accelerate its intrinsic dynamics. In particular, the tremella-like 3D hierarchical structure builds a rich three-phase reaction interface, which improves the mass transfer. Finally, the coupling of CNTs and Ni foam form a unique "meridian" conductive structure that enables rapid electron transfer.

The activity and stability of the oxygen electrocatalyst were tested via cyclic voltammetry and linear sweep voltammetry (LSV) in O$_2$ saturated 0.1 M KOH. As expected, the LSV curves of the OER indicate that the NiCo$_2$O$_4$@MnO$_2$/CNTs-Ni foam exhibits a markedly decreased overpotential ($\eta$, $\eta = E_{j=10}$ -1.23 V, $E_{j=10}$: the OER potential at 10 mA cm$^{-2}$) for the OER of 270 mV in comparison to the Co$_3$O$_4$@MnO$_2$/CNTs-Ni foam (480 mV), NiCo$_2$O$_4$/MnO$_2$-CNTs (510 mV) and NiCo$_2$O$_4$ (590 mV) [Figure 3A]. This overpotential is also 300 mV lower than that of commercial Pt/C-RuO$_2$ catalysts [Supplementary Figure 5A]. This finding demonstrates that the self-supporting electrodes exhibit better OER activity than the powder catalyst, which can be attributed to the 3D hierarchical hollow hybrid structure created by the Ni foam base and the binder-free advantage for the self-supporting electrode[37]. Furthermore, the bimetallic-activated MnO$_2$-based sample also shows a higher OER activity than the single metal-activated MnO$_2$-based catalyst and pure MnO$_2$, indicating that a metal oxide anchored on the MnO$_2$ surface is an effective method to improve the catalytic activity.
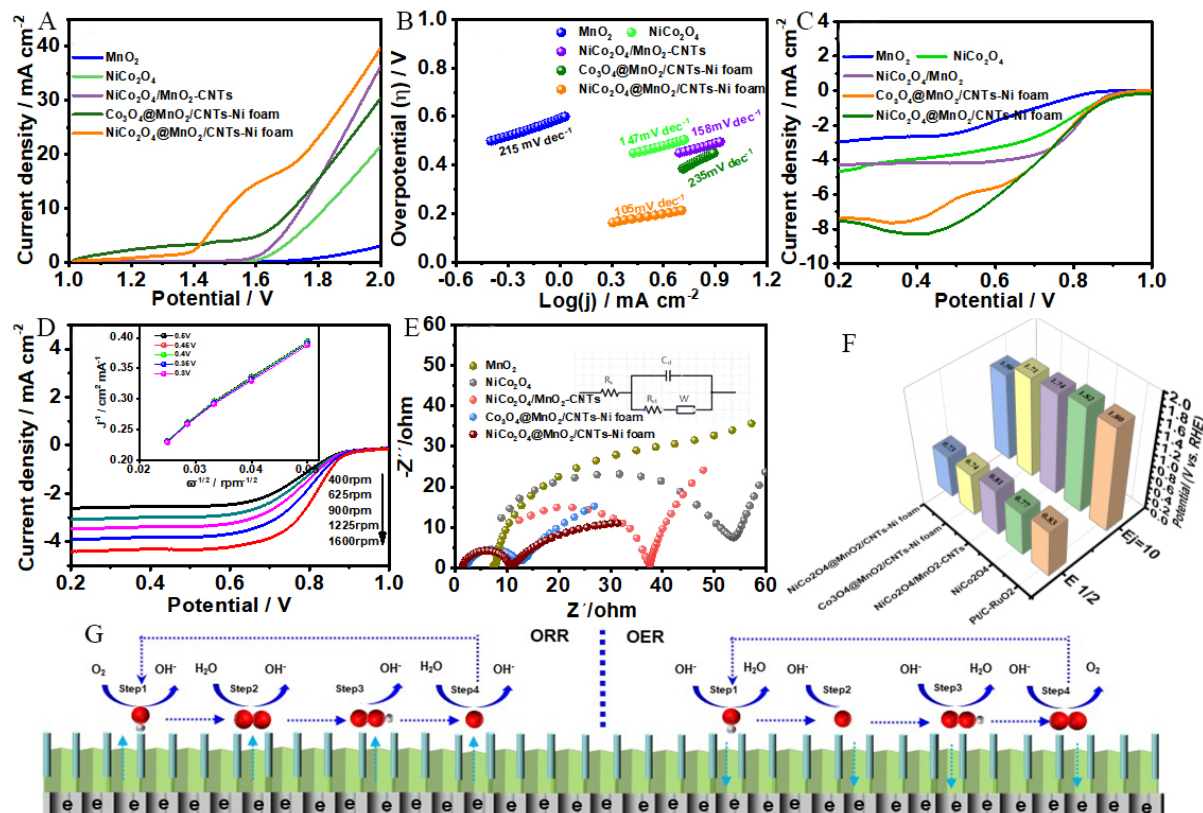
**Figure 3.** (A) OER curves, (B) Tafel slopes, (C) ORR curves, (D) RDE curves at 400-1600 rpm (insert: K-L plots), € EIS curves, and (F) potential gap ($\Delta E$) of ORR and OER for Pt/C-RuO$_2$, NiCo$_2$O$_4$-CNTs, NiCo$_2$O$_4$/MnO$_2$-CNTs, Co$_3$O$_4$@MnO$_2$/CNTs-Ni foam, and NiCo$_2$O$_4$@MnO$_2$/CNTs-Ni foam. (G) Schematic reaction mechanism of ORR and OER electrocatalyzed by NiCo$_2$O$_4$@MnO$_2$/CNTs-Ni foam.

The Tafel slope was also calculated to reveal the reaction kinetics for the OER. As shown in Figure 3B, the small slope (105 mV dec$^{-1}$) further indicates the rapid OER kinetics of the NiCo$_2$O$_4$@MnO$_2$/CNTs-Ni foam, which is faster than the Co$_3$O$_4$@MnO$_2$/CNTs-Ni foam (235 mV dec$^{-1}$), NiCo$_2$O$_4$/MnO$_2$-CNTs (158 mV dec$^{-1}$), NiCo$_2$O$_4$ (147 mV dec$^{-1}$) and MnO$_2$ ((215 mV dec$^{-1}$). In addition to the good OER activity, the NiCo$_2$O$_4$@MnO$_2$/CNTs-Ni foam also shows promising ORR performance [Figure 3C]. Notably, the NiCo$_2$O$_4$@MnO$_2$/CNTs-Ni foam shows a larger limiting current density of 8 mA cm$^{-2}$ than NiCo$_2$O$_4$/MnO$_2$-CNTs (4.4 mA cm$^{-2}$), NiCo$_2$O$_4$ (4.8 mA cm$^{-2}$), MnO$_2$ (3.1 mA cm$^{-2}$) and Pt/C-RuO$_2$ (6 mA cm$^{-2}$) [Supplementary Figure 5B], which further illustrates that the novel hierarchical structure constructed by the self-assembly process of the metal oxide facilitates not only the gas diffusion but also the mass transfer of the ORR[34]. In addition, the onset potential (E$_{onset}$) and half-wave potential (E$_{1/2}$) of NiCo$_2$O$_4$/MnO$_2$-CNTs are 0.87 and 0.81 V, respectively, which are better than for MnO$_2$ (0.82 and 0.67 V) and NiCo$_2$O$_4$ (0.86 and 0.77 V). The high ORR activity of the NiCo$_2$O$_4$@MnO$_2$/CNTs-Ni foam demonstrates that the introduction of bimetallic ions and Ni foam can effectively regulates the electronic structure of the Mn ions and increase the density of the active site (Mn$^{3+}$) in order to form a suitable chemical environment for the oxygen catalytic reaction[10-12,38]. The large limiting current density should be attributed to the 3D hierarchical hollow hybrid structure, which boosts the mass transfer during the ORR.

The electron transfer number of the NiCo$_2$O$_4$@MnO$_2$/CNTs-Ni foam was then calculated using Koutecky-Levich (K-L) plots. The LSV measurement of the sample powder was also carried out at 400-2025 rpm [Figure 3D], and the electron transfer number of NiCo$_2$O$_4$/MnO$_2$-CNTs is in the range of 3.92-3.99,

indicating a four-electron dominant transfer ORR pathway ($O_2$ directly forms $OH^-$). In addition, the semicircle of the Nyquist plot at low frequency corresponds to the Rct, i.e., the charge transfer resistance[39]. The Rct of the $NiCo_2O_4@MnO_2$/CNTs-Ni foam is closer to the $Co_3O_4$/$MnO_2$-CNTs@NF and lower than $NiCo_2O_4$/$MnO_2$-CNTs, $NiCo_2O_4$, and $MnO_2$, suggesting that the tremella-like 3D hierarchical structure and dual heterojunction structure of the $NiCo_2O_4@MnO_2$/CNTs-Ni foam are beneficial to the rapid electron transfer, ion diffusion and product emission [Figure 3E]. Accordingly, the high ORR and OER activities should be due to the unique 3D hierarchical structure effectively promoting electrolyte penetration, $O_2$/$OH^-$ diffusion, and product emission. Furthermore, the abundant $Mn^{3+}$ active sites are activated by bimetallic ions, which shorten the oxygen catalytic reactions distance between the active sites and reactant and reduce the surface activity of $MnO_2$ for the O, OH, and OOH species[13-14,26]. Finally, the CNTs combined with Ni foam form a novel "meridian" conductive structure that enables rapid electron conduction. As a result, the $NiCo_2O_4@MnO_2$/CNTs-Ni foam electrode exhibits the lowest potential gap of ORR and OER ($\Delta E = E_{(j = 10)}-E_{1/2}$, 0.69 V) among all samples [Figure 3F]. In addition, the $\Delta E$ of the $NiCo_2O_4@MnO_2$/CNTs-Ni foam is also smaller than the recently reported work[7,40-46], revealing its high bifunctional oxygen catalytic activity. For better interpreting the influence of the heterojunction structure, ion activation, and Ni substrate of the self-supported electrode, the electrocatalytic mechanism of the ORR and OER occurring in the $NiCo_2O_4$/$MnO_2$-CNTs@Ni foam electrode is illustrated in Figure 3G.

To examine the practical applications of the $NiCo_2O_4@MnO_2$/CNTs-Ni foam electrode, ZABs were assembled with a zinc plate as the anode and the $NiCo_2O_4@MnO_2$/CNTs-Ni foam self-supporting electrode as the air cathode. A ZAB with Pt/C-$RuO_2$ was tested as a contrast. The open-circuit voltage (OCV) of the $NiCo_2O_4@MnO_2$/CNTs-Ni foam battery was 1.51 V, which is superior to the Pt/C-$RuO_2$ counterpart (1.48 V) [Figure 4A]. The power density curves and the charge/discharge polarization curves [Figure 4B] indicate that $NiCo_2O_4$/$MnO_2$-CNTs@NF owned higher peak power density (0.74 V in 303 mA $cm^{-2}$, 226 mW $cm^{-2}$) than Pt/C-$RuO_2$ (0.47 V in 290 mA $cm^{-2}$, 93 mW $cm^{-2}$), thus implied good potential in high-power working conditions. The results of the total area specific resistance (ASR, dV/di) further reveal that $NiCo_2O_4@MnO_2$/CNTs-Ni foam as the cathode exhibits smaller activation polarization, ohmic polarization, and concentration

polarization than Pt/C-$RuO_2$ [Figure 4C]. In addition, the zinc-air battery with $NiCo_2O_4@MnO_2$/CNTs-Ni foam cathode shows a stable discharge performance with a high specific capacity of 814 mAh $g^{-1}$ [Supplementary Figure 6]. Therefore, the high discharge performance of $NiCo_2O_4@MnO_2$/CNTs-Ni foam should be attributed to the high ORR activity (bimetallic-activated $MnO_2$ and dual heterojunction), good conduction (Ni foam and binder-free), and rapid mass transfer (3D tremella-like hierarchical structure). Compared with Pt/C-$RuO_2$, the voltage drop of the battery with the $NiCo_2O_4@MnO_2$/CNTs-Ni foam air electrode was relatively small during constant current discharge measurements, with the current densities varying from 5 to 30 mA $cm^{-2}$ [Figure 4D], indicating its excellent rate capability. Discharge voltage would recover entirely when the current density was looped to 5 mA $cm^{-2}$, which verified its satisfactory reversibility.

To further evaluate the charge-discharge potential and cycling stability, the galvanodynamic method and discharge-charge cycling testing were performed, respectively. As shown in Figure 4E, the $NiCo_2O_4@MnO_2$/CNTs-Ni foam shows a lower charge-discharge potential at a larger current density than Pt/C-$IrO_2$. The ZAB based on the $NiCo_2O_4@MnO_2$/CNTs-Ni foam also displayed better cycling stability (165 h) with a durable and small charge-discharge voltage gap of 0.72 V than Pt/C-$RuO_2$ (6 h, 0.82 V) [Figure 4F]. For the $NiCo_2O_4@MnO_2$/CNTs-Ni foam, the voltage gap of the ZAB based on the $NiCo_2O_4@MnO_2$/CNTs-Ni foam increased from 0.72 to 0.77 V after a continuous cycling operation for 150 h, showing that good long-term
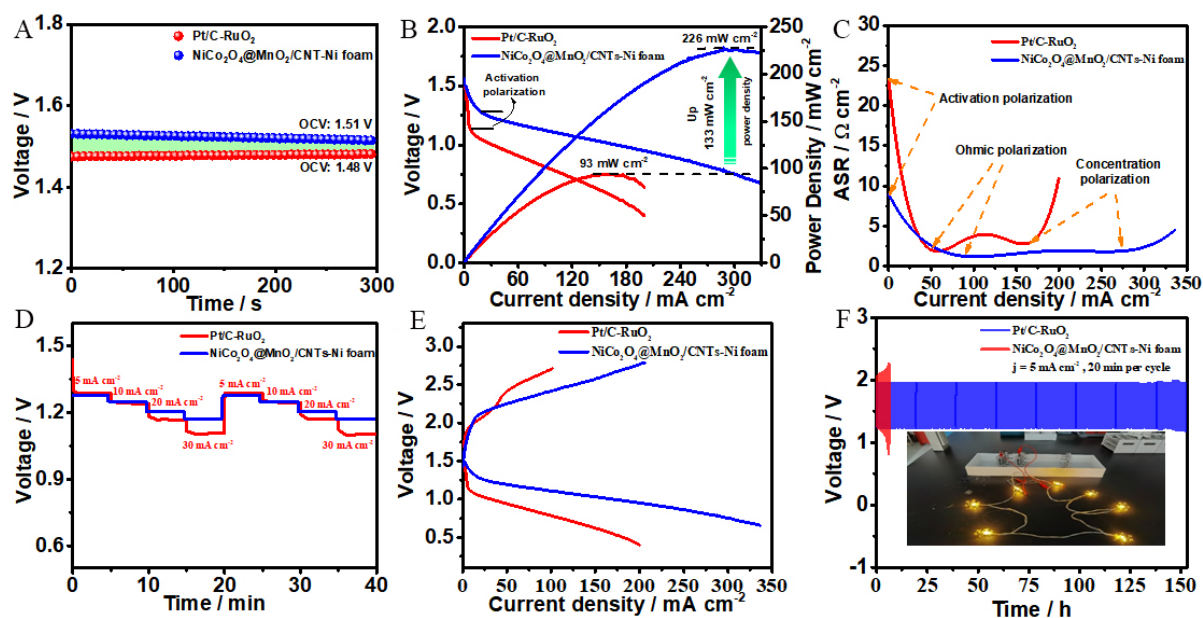
**Figure 4.** ZAB using Pt/C-RuO$_2$ and NiCo$_2$O$_4$@MnO$_2$/CNTs-Ni foam. (A) OCV curves. (B) Polarization curves and corresponding power density plots. (C) Total ASR curves. (d) Different rate discharge cycling curves at different current densities (5-30 mA cm$^{-2}$). (E) Charge and discharge polarization curves. (F) Charge-discharge cycles at 5 mA cm$^{-2}$ (insert: a small bulb powered by a ZAB in series).

charge-discharge cycling performance. In comparison, the Pt/C-RuO$_2$ electrode showed a fast performance degradation after 7 h. Finally, the morphology and electron structure of the NiCo$_2$O$_4$@MnO$_2$/CNTs-Ni foam were obtained by using SEM and XPS after the long-term stability testing; the result proves the self-supporting 3D hierarchical hollow hybrid structure and the stable active sites greatly improve the catalyst lifetime [Supplementary Figure 7]. The ZAB based on the NiCo$_2$O$_4$@MnO$_2$/CNTs-Ni foam air electrode shows better primary/rechargeable battery performance with higher power density and smaller charge-discharge voltage gap than the most recently reported NiCo$_2$O$_4$/MnO$_2$-based bifunctional electrodes [Supplementary Table 1]. Simultaneously, the ZAB in series can power multiple small bulbs, showing good practical application prospects (insert of Figure 4F).

## CONCLUSIONS

In summary, a NiCo$_2$O$_4$@MnO$_2$/CNTs-Ni foam self-supported electrode was successfully designed and synthesized by a facial hydrothermal self-assembly process. The as-synthesized NiCo$_2$O$_4$@MnO$_2$/CNTs-Ni foam self-supported electrode has a unique tremella-like 3D hierarchical structure with an abundant heterojunction and evolves rich Mn$^{3+}$ active sites. The unique hierarchical structure effectively promotes electrolyte penetration, reactant (O$_2$ and OH$^-$) diffusion, and product emission. In addition, the abundant Mn$^{3+}$ active sites activated by bimetallic ions effectively improve the oxygen catalytic intrinsic performance. Furthermore, the steric hindrance effect and providing self-assembly site mechanism of the Ni substrate were studied. The introduction of Ni foam can significantly avoid the agglomeration of metal oxides and induce the evolution of the nanoparticles on the surface of MnO$_2$ into two-dimensional nanosheets, which realize the rapid formation of the abundant three-phase reaction interfaces. As expected, the NiCo$_2$O$_4$@MnO$_2$/CNTs-Ni foam demonstrates a promising ORR and OER performance with high catalytic activity (total overpotential of 0.67 V) and the rapid intrinsic kinetics (a small Tafel slope of 105 mV dec$^{-1}$). In addition, the ZABs with the NiCo$_2$O$_4$@MnO$_2$/CNTs-Ni foam cathode also show a high peak power density of 226 mW cm$^{-2}$, a large specific capacity of 814 mAh g$^{-1}$ and a stable charge-discharge cycles with low voltage gap of 0.72 V for 165 h at 5 mA cm$^{-2}$. These findings provide inspiration for the design of novel

performance-oriented Mn-based self-supported electrodes for wider applications in metal-air batteries.

## DECLARATIONS

### Authors' contributions
Methodology, formal analysis, investigation, writing manuscript: Yin Z, He R
Validation, resources, formal analysis: Chen J, Wang Y
Methodology, visualization, investigation: Ye X, Huang H, Xue H
Project administration, conceptualization, funding acquisition, supervision, writing manuscript: Xu N, Qiao J

### Availability of data and materials
The data supporting our work can be found in the supplementary information.

### Conflicts of interest
All authors declared that there are no conflicts of interest.

### Ethical approval and consent to participate
Not applicable.

### Consent for publication
Not applicable.

### Copyright
© The Author(s) 2022.

## REFERENCES

1.  Bae J, Shin D, Jeong H, et al. Facet-dependent Mn doping on shaped $Co_3O_4$ crystals for catalytic oxidation. *ACS Catal* 2021;11:11066-74.  DOI
2.  Chen C, Su H, Lu L, et al. Interfacing spinel $NiCo_2O_4$ and NiCo alloy derived N-doped carbon nanotubes for enhanced oxygen electrocatalysis. *Chem Eng J* 2021;408:127814.  DOI
3.  Liu Y, Deng H, Lu Z, Zhong X, Zhu Y. The study of $MnO_2$ with different crystalline structures for U(VI) elimination from aqueous solution. *J Mol Liquids* 2021;335:116296.  DOI
4.  Xiao X, Hu X, Liang Y, et al. Anchoring $NiCo_2O_4$ nanowhiskers in biomass-derived porous carbon as superior oxygen electrocatalyst for rechargeable Zn-air battery. *J Power Sources* 2020;476:228684.  DOI
5.  Li H, Ma L, Han C, et al. Advanced rechargeable zinc-based batteries: recent progress and future perspectives. *Nano Energy* 2019;62:550-87.  DOI
6.  Pan J, Xu YY, Yang H, Dong Z, Liu H, Xia BY. Advanced architectures and relatives of air electrodes in Zn-air batteries. *Adv Sci (Weinh)* 2018;5:1700691.  DOI  PubMed  PMC
7.  Yin M, Miao H, Chen B, et al. Self-supported metal sulfide electrode for flexible quasi-solid-state zinc-air batteries. *J Alloys Compd* 2021;878:160434.  DOI
8.  Cheng H, Chen JM, Li QJ, et al. A modified molecular framework derived highly efficient Mn-Co-carbon cathode for a flexible Zn-air battery. *Chem Commun (Camb)* 2017;53:11596-9.  DOI  PubMed
9.  Yang Z, Zheng C, Wei Z, et al. Multi-dimensional correlation of layered Li-rich Mn-based cathode materials. *Energy Mater* 2022;2:200006.  DOI
10. Xu N, Liu J, Qiao J, Huang H, Zhou X. Interweaving between $MnO_2$ nanowires/nanorods and carbon nanotubes as robust multifunctional electrode for both liquid and flexible electrochemical energy devices. *J Power Sources* 2020;455:227992.  DOI

11.   Xu N, Nie Q, Luo L, et al. Controllable hortensia-like $MnO_2$ synergized with carbon nanotubes as an efficient electrocatalyst for long-term metal-air batteries. *ACS Appl Mater Interfaces* 2019;11:578-87.  DOI  PubMed

12.   Lee S, Nam G, Sun J, et al. Enhanced intrinsic catalytic activity of λ-$MnO_2$ by electrochemical tuning and oxygen vacancy generation. *Angew Chem Int Ed* 2016;55:8599-604.  DOI  PubMed

13.   Xu N, Zhang Y, Wang M, et al. High-performing rechargeable/flexible zinc-air batteries by coordinated hierarchical Bi-metallic electrocatalyst and heterostructure anion exchange membrane. *Nano Energy* 2019;65:104021.  DOI

14.   Xu N, Zhang Y, Wang Y, et al. Hierarchical bifunctional catalysts with tailored catalytic activity for high-energy rechargeable Zn-air batteries. *Appl Energy* 2020;279:115876.  DOI

15.   Singh A, Ojha AK. Designing vertically aligned porous $NiCo_2O_4$@$MnMoO_4$ Core@Shell nanostructures for high-performance asymmetric supercapacitors. *J Colloid Interface Sci* 2020;580:720-9.  DOI  PubMed

16.   Li A, Kong S, Guo C, et al. Enhancing the stability of cobalt spinel oxide towards sustainable oxygen evolution in acid. *Nat Catal* 2022;5:109-18.  DOI

17.   Xu N, Cai Y, Peng L, et al. Superior stability of a bifunctional oxygen electrode for primary, rechargeable and flexible Zn-air batteries. *Nanoscale* 2018;10:13626-37.  DOI  PubMed

18.   Wang XT, Ouyang T, Wang L, Zhong JH, Ma T, Liu ZQ. Redox-Inert $Fe^{3+}$ ions in octahedral sites of Co-Fe spinel oxides with enhanced oxygen catalytic activity for rechargeable zinc-air batteries. *Angew Chem Int Ed* 2019;58:13291-6.  DOI  PubMed

19.   Gangadharan PK, Bhange SN, Kabeer N, Illathvalappil R, Kurungot S. $NiCo_2O_4$ nanoarray on CNT sponge: a bifunctional oxygen electrode material for rechargeable Zn–air batteries. *Nanoscale Adv* 2019;1:3243-51.  DOI

20.   Kumar R. $NiCo_2O_4$ nano-/microstructures as high-performance biosensors: a review. *Nanomicro Lett* 2020;12:122.  DOI  PubMed  PMC

21.   Yang C, Gao N, Wang X, et al. Phosphate boosting stable efficient seawater splitting on porous NiFe (oxy)hydroxide@$NiMoO_4$ Core-Shell micropillar electrode. *Energy Mater* 2021;1:100015.  DOI

22.   Ma TY, Dai S, Qiao SZ. Self-supported electrocatalysts for advanced energy conversion processes. *Mater Today* 2016;19:265-73.  DOI

23.   Ye L, Hong Y, Liao M, et al. Recent advances in flexible fiber-shaped metal-air batteries. *Energy Stor Mater* 2020;28:364-74.  DOI

24.   Pei Z, Yuan Z, Wang C, et al. A flexible rechargeable zinc-air battery with excellent low-temperature adaptability. *Angew Chem Int Ed* 2020;59:4793-9.  DOI  PubMed

25.   Wang B, Chen Y, Wang X, et al. A microwave-assisted bubble bursting strategy to grow $Co_8FeS_8$/CoS heterostructure on rearranged carbon nanotubes as efficient electrocatalyst for oxygen evolution reaction. *J Power Sources* 2020;449:227561.  DOI

26.   Xu N, Zhang Y, Zhang T, Liu Y, Qiao J. Efficient quantum dots anchored nanocomposite for highly active ORR/OER electrocatalyst of advanced metal-air batteries. *Nano Energy* 2019;57:176-85.  DOI

27.   Xu N, Liu Y, Zhang X, et al. Self-assembly formation of Bi-functional $Co_3O_4$/$MnO_2$-CNTs hybrid catalysts for achieving both high energy/power density and cyclic ability of rechargeable zinc-air battery. *Sci Rep* 2016;6:33590.  DOI  PubMed  PMC

28.   Xu N, Wilson JA, Wang Y, et al. Flexible self-supported bi-metal electrode as a highly stable carbon- and binder-free cathode for large-scale solid-state zinc-air batteries. *Appl Catal B-Environ* 2020;272:118953.  DOI

29.   Wang A, Hu Y, Wang H, et al. Activating inverse spinel $NiCo_2O_4$ embedded in N-doped carbon nanofibers via Fe substitution for bifunctional oxygen electrocatalysis. *Mater Today Phys* 2021;17:100353.  DOI

30.   Ma R, Lin G, Ju Q, et al. Edge-sited $Fe-N_4$ atomic species improve oxygen reduction activity via boosting $O_2$ dissociation. *Appl Catal B: Environ* 2020;265:118593.  DOI

31.   Singh T, Das C, Bothra N, et al. MOF Derived $Co_3O_4$@Co/NCNT nanocomposite for electrochemical hydrogen evolution, flexible zinc-air batteries, and overall water splitting. *Inorg Chem* 2020;59:3160-70.  DOI  PubMed

32.   Wang Z, Ang J, Liu J, et al. FeNi alloys encapsulated in N-doped CNTs-tangled porous carbon fibers as highly efficient and durable bifunctional oxygen electrocatalyst for rechargeable zinc-air battery. *Appl Catal B: Environ* 2020;263:118344.  DOI

33.   Xie W, Li J, Song Y, Li S, Li J, Shao M. Hierarchical carbon microtube@nanotube core-shell structure for high-performance oxygen electrocatalysis and Zn-air battery. *Nanomicro Lett* 2020;12:97.  DOI  PubMed  PMC

34.   Zhang X, Han X, Jiang Z, et al. Atomically dispersed hierarchically ordered porous Fe-N-C electrocatalyst for high performance electrocatalytic oxygen reduction in Zn-air battery. *Nano Energy* 2020;71:104547.  DOI

35.   Zheng X, Cao X, Sun Z, et al. Indiscrete metal/metal-N-C synergic active sites for efficient and durable oxygen electrocatalysis toward advanced Zn-air batteries. *Appl Catal B: Environ* 2020;272:118967.  DOI

36.   Wang Q, Xue Y, Sun S, Yan S, Miao H, Liu Z. Facile synthesis of ternary spinel Co-Mn-Ni nanorods as efficient bi-functional oxygen catalysts for rechargeable zinc-air batteries. *J Power Sources* 2019;435:226761.  DOI

37.   Deng Y, Jiang Y, Luo D, et al. Hierarchical porous double-shelled electrocatalyst with tailored lattice alkalinity toward bifunctional oxygen reactions for metal-air batteries. *ACS Energy Lett* 2017;2:2706-12.  DOI

38.   Su HY, Gorlin Y, Man IC, et al. Identifying active surface phases for metal oxide electrocatalysts: a study of manganese oxide bi-functional catalysts for oxygen reduction and water oxidation catalysis. *Phys Chem Chem Phys* 2012;14:14010-22.  DOI  PubMed

39.   Chen Z, Yu A, Ahmed R, Wang H, Li H, Chen Z. Manganese dioxide nanotube and nitrogen-doped carbon nanotube based composite bifunctional catalyst for rechargeable zinc-air battery. *Electrochim Acta* 2012;69:295-300.  DOI

40.   Han C, Zhang T, Li J, Li B, Lin Z. Enabling flexible solid-state Zn batteries via tailoring sulfur deficiency in bimetallic sulfide nanotube arrays. *Nano Energy* 2020;77:105165.  DOI

41.  Han J, Meng X, Lu L, Wang ZL, Sun C. Triboelectric nanogenerators powered electrodepositing tri-functional electrocatalysts for water splitting and rechargeable zinc-air battery: a case of Pt nanoclusters on NiFe-LDH nanosheets. *Nano Energy* 2020;72:104669. DOI

42.  Wang Y, Li Z, Zhang P, et al. Flexible carbon nanofiber film with diatomic Fe-Co sites for efficient oxygen reduction and evolution reactions in wearable zinc-air batteries. *Nano Energy* 2021;87:106147.  DOI

43.  Wang Z, Huang J, Wang L, et al. Cation-tuning induced d-band center modulation on Co-based spinel oxide for oxygen reduction/evolution reaction. *Angew Chem Int Ed* 2022;61:e202114696.  DOI  PubMed

44.  Yan L, Xu Z, Hu W, Ning J, Zhong Y, Hu Y. Formation of sandwiched leaf-like CNTs-Co/ZnCo$_2$O$_4$@NC-CNTs nanohybrids for high-power-density rechargeable Zn-air batteries. *Nano Energy* 2021;82:105710.  DOI

45.  Zhang Z, Sun H, Li J, et al. S-doped CoMn$_2$O$_4$ with more high valence metallic cations and oxygen defects for zinc-air batteries. *J Power Sources* 2021;491:229584.  DOI

46.  Tao B, He J, Miao F, Zhang Y. MnO$_2$/NiCo$_2$O$_4$ loaded on nickel foam as a high-performance electrode for advanced asymmetric supercapacitor. *Vacuum* 2022;195:110668.  DOI